International Journal of Solids and Structures 49 (2012) 2830–2838

Contents lists available at SciVerse ScienceDirect

International Journal of Solids and Structures

journal homepage: www.elsevier.com/locate/ijsolstr

Dynamic buckling of an inclined strut

G.J. McShane *, S.M. Pingle, V.S. Deshpande, N.A. Fleck

Dept. of Engineering, University of Cambridge, Trumpington Street, Cambridge CB2 1PZ, UK

ARTICLE INFO

Article history:
Available online 13 April 2012

Keywords:
Dynamic buckling
Metallic lattice
Sandwich
Impact
Blast

ABSTRACT

The dynamic compressive response of a sandwich plate with a metallic corrugated core is predicted. The back face of the sandwich plate is held fixed whereas the front face is subjected to a uniform velocity, thereby compressing the core. Finite element analysis is performed to investigate the role of material inertia, strain hardening and strain rate hardening upon the dynamic collapse of the corrugated core. Three classes of collapse mode are identified as a function of impact velocity: (i) a three-hinge plastic buckling mode of wavelength equal to the strut length, similar to the quasi-static mode, (ii) a 'buckle-wave' regime involving inertia-mediated plastic buckling of wavelength less than that of the strut length, and (iii) a 'stubbing' regime, with shortening of the struts by local fattening at the front face. The presence of strain hardening reduces the regime of dominance of the stubbing mode. The influence of material strain rate sensitivity is evaluated by introducing strain rate dependent material properties representative of type 304 stainless steel. For this choice of material, strain rate sensitivity has a more minor influence than strain hardening, and consequently the dynamic collapse strength of a corrugated core is almost independent of structural dimension.

1. Introduction

Sandwich plates with metallic lattice cores have recently emerged as promising candidates for lightweight structures: the sandwich construction combines high stiffness and strength along with high resistance to blast loading (Fleck and Deshpande, 2004; Xue and Hutchinson, 2004; Radford et al., 2006; Rathbun et al., 2006). The selection of a suitable lattice core requires an understanding of the dynamic collapse of the core members, typically rods or plates oriented either normal to the face sheets (as in the I-core and some honeycomb designs) or at an angle (as in the corrugated and pyramidal truss cores).

There exists in the literature a good understanding of the role of material inertia upon the axial collapse of rods and tubes, see for example the reviews by Jones (1989, 2003) and Reid (1993) and the recent paper on buckle-wave propagation by Vaughn and Hutchinson (2006). Recently, a number of studies have explored the dynamic collapse of sandwich cores with vertical members such as the I-core (Ferri et al., 2006) and the square honeycomb (Xue and Hutchinson, 2006; Radford et al., 2007). The main phenomena that have been identified are micro-inertial stabilisation against buckling (Calladine and English, 1984), plastic shock wave effects and imperfection sensitivity. Much less is known about the dynamic response of sandwich cores with inclined struts. Recently, Tilbrook et al. (2007) have measured and analysed the dynamic response of a corrugated core made from 304 stainless steel, while Lee et al. (2006) have performed a similar study for the pyramidal core. Two regimes were identified, corresponding to micro-inertia stabilisation and shock-wave propagation. However, in both of these studies, a limited number of geometries were considered. The focus of the present study is to generate dynamic buckling maps for the dynamic compressive response of the corrugated core. Finite element analysis is performed to investigate the role of material inertia, strain hardening and strain rate hardening upon the dynamic collapse of the corrugated core.

We begin by reviewing briefly the main phenomena associated with dynamic plastic buckling of a column impacted at one end and rigidly supported at the other.

(i) Inertia stabilisation against buckling at low impact velocities

At low impact velocities, much less than that of axial plastic waves, axial equilibrium exists and shock wave effects are negligible. However, the lateral inertia of a column stabilises it against buckling. The effect is large, particularly for elastic buckling, as investigated by Hoff (1951). Calladine and English (1984) considered the equivalent rigid-plastic problem and showed that plastic buckling is delayed by lateral inertia so that the early stage of deformation is by axial shortening. This was extended to the case of elastic–plastic, strain hardening and rate dependent solids by Karagiozova and Jones (1995), Su et al. (1995a,b) and Hönig and Stronge (2000). A series of classic experiments to elucidate the dynamic plastic buckling modes were reported by Abrahamson and

* Corresponding author.
E-mail address: gjm31@cam.ac.uk (G.J. McShane).

0020-7683/$ - see front matter © 2012 Elsevier Ltd. All rights reserved.
http://dx.doi.org/10.1016/j.ijsolstr.2012.03.045

Goodier (1966). Karagiozova and Jones (1996) show that material inertia, loading conditions and boundary conditions all influence the dynamic buckling patterns in rods impacted axially.

(ii) Buckle waves at moderate impact velocities

At moderate impact speeds, an axial plastic shock wave propagates along the column, and behind its wave front the column buckles plastically (Vaughn et al., 2005; Vaughn and Hutchinson, 2006). Since the effective length of the buckling column increases with time, we adopt the language of Vaughn and Hutchinson (2006) and refer to this phenomenon as a 'buckle-wave'.

(iii) Axial plastic shock wave at high velocities

Consider now the case where the impact velocity exceeds that of axial plastic waves. A shock develops at the impacted end, and the column fattens and shortens at the impacted end, as described by Taylor (1948). Consequently, we refer to this as the 'Taylor impact' regime.

Metallic foams as well as other cellular cores such as honeycombs also undergo inertial stabilisation effects by mechanisms analogous to those listed above; see the discussion in Deshpande and Fleck (2000) and Tan et al. (2005a, 2005b). The broad aim of the present paper is to investigate these inertial stabilisation effects for a prismatic corrugated core and systematically map the regimes of dynamic collapse for this core. Finite element analysis is used to calculate the core response to constant velocity compression. The effect of compression velocity, strut slenderness, material strain hardening and material strain rate sensitivity are considered in turn. Of particular interest are the reaction forces exerted by the collapsing strut upon the front and back face sheets (considered here to be rigid).

The paper is organized as follows. A representative inclined strut is sandwiched between two face-sheets; the front face sheet is subjected to a constant velocity V_0 while the back face sheet rests on a rigid support, see Fig. 1. In Section 2, the inclined strut geometry, boundary conditions and material properties are defined, and details of the finite element modelling procedure are given. In Section 3, results are presented which illustrate the dynamic buckling modes of the strut for the simplest material model: the elastic, ideally plastic solid, lacking both strain hardening and significant strain rate sensitivity. Collapse mechanism maps are constructed with axes representing the strut slenderness (related directly to the relative density of the lattice core) and the compression velocity V_0. In Sections 4 and 5, the role of strain hardening and strain rate sensitivity are assessed, respectively. With the introduction of strain rate sensitivity, the physical dimensions of the strut become important. Finite element calculations are included for 'laboratory scale' and 'full scale' metallic lattices to assess the scaling effects. These calculations are useful in order to assess the degree to which the strain rate sensitivity of laboratory-scale specimens carries over to the full-scale counterparts.

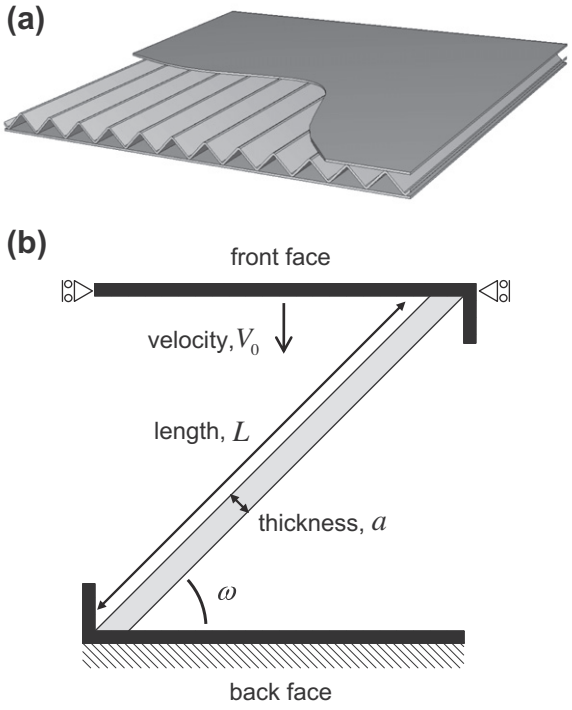

Fig. 1. (a) A corrugated core sandwich panel, and (b) an idealised unit cell, a single strut inclined at an angle ω attached at either end to rigid face sheets.

2. Outline of the finite element modelling procedure

The finite strain version of the commercially available finite element code ABAQUS is used to calculate the compressive response of the corrugated core. Dynamic results are obtained using ABAQUS/Explicit, and the quasi-static collapse is calculated using ABAQUS/Standard. Details of the finite element model and the material properties are as follows.

2.1. Inclined strut geometry and boundary conditions

The corrugated core sandwich panel of the current investigation is shown in Fig. 1. A metallic folded plate core is bonded to solid metallic face sheets, providing a stiff, lightweight structural panel. Herein, only the compressive deformation of the core is considered. The face sheets are considered to be sufficiently strong so as to behave in a rigid manner, and are constrained to approach each other without relative sliding.

To facilitate the analysis, an idealised unit cell is considered, as shown in Fig. 1b. Planar deformation is assumed, such that plane strain conditions prevail along the prismatic direction, and consequently results are presented assuming unit depth in the prismatic direction. Hard but frictionless contacts are assumed between all surfaces in the model. The representative strut has length L, width a and is inclined at an angle ω to the horizontal. The length L is varied to give aspect ratios in the range $20 \leqslant L/a \leqslant 100$ to cover the practical range of corrugated core topologies. The relative density $\bar{\rho}$ of the corrugated core constructed from this unit cell is given by

$$\bar{\rho} = \left(1 + \frac{L}{a}\sin\omega\cos\omega\right)^{-1}, \tag{1a}$$

which reduces to

$$\bar{\rho} \approx \frac{2a}{L\sin 2\omega}, \tag{1b}$$

in the limit $a/L \to 0$. For example, the choice $L/a = 40$ and $\omega = 45°$ corresponds to a core of relative density $\bar{\rho} = 5\%$. Only an inclination angle $\omega = 45°$ will be considered in the present study. We shall subsequently refer to the cores via their relative density (or equivalently slenderness ratio) as this is the standard metric used to define a cellular material under quasi-static loading. We recognise that this parameter alone may be insufficient to fully characterise the dynamic performance of the core.

The back face sheet is fully clamped against displacement and rotation, see Fig. 1b. In contrast, the front face is driven at constant velocity V_0 in order to compress the core, and consequently the nominal core compressive strain increases with time t according to

$$\bar{\varepsilon} = \frac{V_0 t}{L\sin\omega}. \tag{2}$$

In order to minimise initial transient oscillations in the computed face sheet reaction forces, the front face velocity is ramped

smoothly from zero to the target value V_0 over a time t_r in such a way as to give no discontinuities in either the velocity or the acceleration of the face sheet (the ABAQUS 'smooth step' time-dependent amplitude is used). Define the longitudinal plastic wave speed of the strut material as c_{pl}. Then, the ramp time is taken to be

$$t_r = \frac{a}{5c_{pl}}, \tag{3}$$

and is chosen to be sufficiently small such that the crushing response of the core is essentially at constant velocity V_0 throughout most of the collapse event.

2.2. Finite element discretization

The geometry is discretized using four-noded plane strain quadrilateral elements (CPE4R in ABAQUS notation), with 20 elements across the width of the strut. A preliminary investigation was performed to determine the sensitivity of the response to the initial geometric imperfection. Ferri et al. (2006) have shown that finite element predictions of the dynamic collapse of the I-core structure (equivalent to the present geometry with $\omega = 90°$) are sensitive to the initial imperfection. However, for the inclined strut we find negligible imperfection sensitivity during dynamic compression. The inclined strut is, however, imperfection sensitive during *quasi-static* collapse, consistent with the findings of Côté et al. (2006). We therefore introduce a small initial geometric imperfection in the form of the first static buckling mode with amplitude $0.03a$ in all calculations which follow.

2.3. Material properties

An elastic–plastic constitutive model is employed for the core. The material model is an idealised representation of the properties of type 304 stainless steel. This material has been used in several recent experimental studies on the dynamic collapse of metallic lattices, such as Radford et al (2006) and Tilbrook et al (2007). The Young's modulus is $E = 200$ GPa and Poisson's ratio is $\nu = 0.3$. J2 flow theory is used with an initial uniaxial yield stress $\sigma_Y = 200$ MPa. Two levels of strain hardening are considered: (i) perfect plasticity ($E_t = 0$) and (ii) isotropic hardening with constant tangent modulus $E_t = E/100 = 2$ GPa under uniaxial deformation; this is a realistic value for stainless steel. The density is $\rho = 8000$ kg m^{-3}. Note that the current analysis is performed under plane strain conditions wherein the effective Young's modulus $\overline{E} = E/(1-\nu^2) = 220$ GPa, yield stress $\bar{\sigma}_Y = 2\sigma_Y/\sqrt{3} = 231$ MPa and tangent modulus $\overline{E}_t = 4E_t/3 = 2.67$ GPa.

In order to resolve any shocks during the dynamic deformation, all calculations feature strain rate dependent plasticity. The dynamic strain hardening behaviour is given by the true stress versus true strain relation

$$\sigma(\varepsilon_{pl}, \dot{\varepsilon}_{pl}) = R(\dot{\varepsilon}_{pl})\sigma_0(\varepsilon_{pl}), \tag{4}$$

where $\sigma_0(\varepsilon_{pl})$ is the quasi-static response and $R(\dot{\varepsilon}_{pl})$ is a strain-rate dependent multiplier. In the finite element simulations, it is necessary to include a sufficient degree of strain rate sensitivity in order to obtain a shock wave of finite width. Two choices of strain rate sensitivity are adopted in the simulations:

(i) A rate sensitivity which is just sufficient to give a shock wave width of 10 elements. This is achieved by taking

$$R(\dot{\varepsilon}_{pl}) = 1 + \frac{10d\dot{\varepsilon}_{pl}}{c_{pl}}, \tag{5}$$

where d is the finite element size, as discussed by Radford et al. (2005). We note that this estimate of shock width is derived using one-dimensional wave theory. The plastic compression of the inclined strut is significantly more complicated with flexure and shearing. In the finite element calculations, $d = 0.05$ mm and $c_{pl} = \sqrt{\bar{\sigma}_y/\rho} = 170$ ms^{-1} were taken, giving $R = 1.03$ at a strain rate $\dot{\varepsilon}_{pl} = 10^4$ s^{-1}.

(ii) The measured strain rate sensitivity $R(\dot{\varepsilon}_{pl})$ for 304 stainless steel. Tabulated values of $R(\dot{\varepsilon}_{pl})$ are employed, from the results of Stout and Follansbee (1986) as given in Fig. 2 of Radford et al. (2007). Within one-dimensional wave theory this choice of strain rate sensitivity gives a more smeared-out shock wave than the choice (i).

3. Collapse response for a non-hardening solid

The collapse response of the corrugated core with inclination angle $\omega = 45°$ is now described for an elastic, ideally plastic solid with low strain rate sensitivity, as prescribed by Eq. (5). We first describe the modes of dynamic collapse of the corrugated core, and relate these to the compression velocity and the slenderness L/a. Finally, the results for a range of slenderness and compression velocity are assembled into a collapse mechanism regime map.

3.1. Regimes of collapse

We first consider the regimes of compressive collapse and the influence of compression velocity and slenderness. The rate of core compression is defined in terms of the non-dimensional front face sheet velocity $V_0/(c_{pl}\sin\omega)$, where the plastic wave speed for the non-hardening solid, $c_{pl} = \sqrt{\bar{\sigma}_Y/\rho}$. Dynamic calculations are performed using ABAQUS/Explicit for velocities in the range $V_0/(c_{pl}\sin\omega) = 8\times10^{-3} - 1.7$ (equivalent to $V_0 = 1 - 200$ ms^{-1}). In addition, the quasi-static collapse response is calculated using ABAQUS/Standard. The evolution of the deformation patterns and the face sheet reaction forces are obtained up to large nominal compressive strains ($\bar{\varepsilon}$). We consider two strut geometries: a stocky strut with $L/a = 20$, which corresponds to a core of relative density $\bar{\rho} = 9\%$, and a slender strut with $L/a = 60$, implying $\bar{\rho} = 3\%$.

The transient front and back face sheet reaction forces F are shown as a function of nominal core compression $\bar{\varepsilon}$ for the two cases in Figs. 2 and 3, respectively. Note that F is the normal component of reaction force for a single unit cell, per unit length in the prismatic direction. We normalise the force F by the static yield load $\bar{\sigma}_Y a\sin\omega$, and deformed shapes of the inclined strut at selected values of $\bar{\varepsilon}$ are included in Figs. 2 and 3. Three collapse modes are identified, in order of increasing compression velocity.

(1) *Elastic/plastic buckling.* At the low velocity, the strut collapses by buckling with a wavelength equal to L, the strut length. Axial equilibrium is maintained during collapse, with front and back face sheet forces equal. Elastic buckling occurs at large L/a, whereas plastic buckling occurs for stocky struts. Subsequent to buckling, deformation proceeds by the rotation of three static plastic hinges, at the face sheets and at the centre of the strut. This regime is observed from quasi-static compression up to front face sheet velocities of the order $V_0/(c_{pl}\sin\omega) \approx 0.05$.

Figs. 2(a) and 3(a) show results for the inclined strut compressed (i) quasi-statically and (ii) at a front face sheet velocity $V_0/(c_{pl}\sin\omega) = 8.3\times10^{-3}$ (equivalent to $V_0 = 1$ ms^{-1}) for aspect ratios $L/a = 20$ and 60, respectively. For the stocky strut with $L/a = 20$ (Fig. 2a), plastic buckling occurs at both speeds, and the collapse forces are nearly identical, with a peak value of $F/(\bar{\sigma}_Y a\sin\omega) = 1.0$. In contrast, the slender strut of $L/a = 60$ buckles elastically at quasi-static rates, with a peak load of $F/(\bar{\sigma}_Y a\sin\omega) = 0.6$ (see Fig. 3a), and buckles plastically at $V_0/(c_{pl}\sin\omega) = 8.3\times10^{-3}$, due to lateral inertia stabilisation, as discussed by Hoff (1951) and Calladine and English (1984).

The 3-hinge buckling mode at $\bar{\varepsilon} = 0.15$ is shown for the choice $V_0/(c_{pl}\sin\omega) = 8.3\times10^{-3}$ in Figs. 2(a) and 3(a). For the stocky

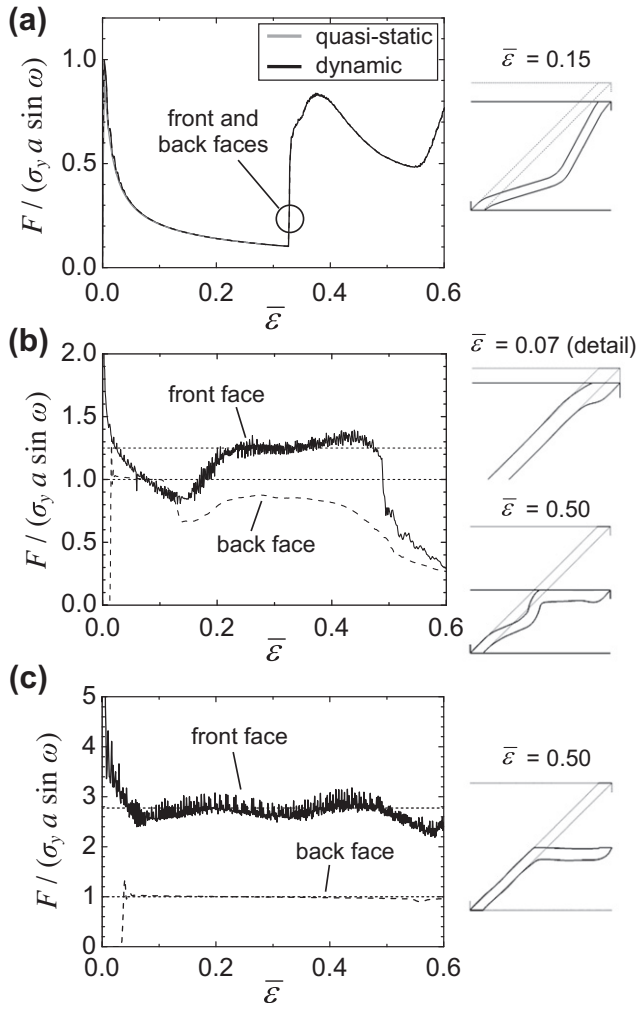

Fig. 2. Variation in the face sheet reaction force F during dynamic collapse of the corrugated core with $L/a = 20$, and $V_0/(c_{pl} \sin \omega)$ equal to (a) 0.0083, (b) 0.50 and (c) 1.3. The quasi-static result is also plotted in (a). Selected deformed shapes are shown adjacent to the corresponding plot. The predictions of the 'stubbing' model for the front and back faces (Eqs. (6) and (7)) are shown as dotted lines in (b) and (c). Non hardening plasticity.

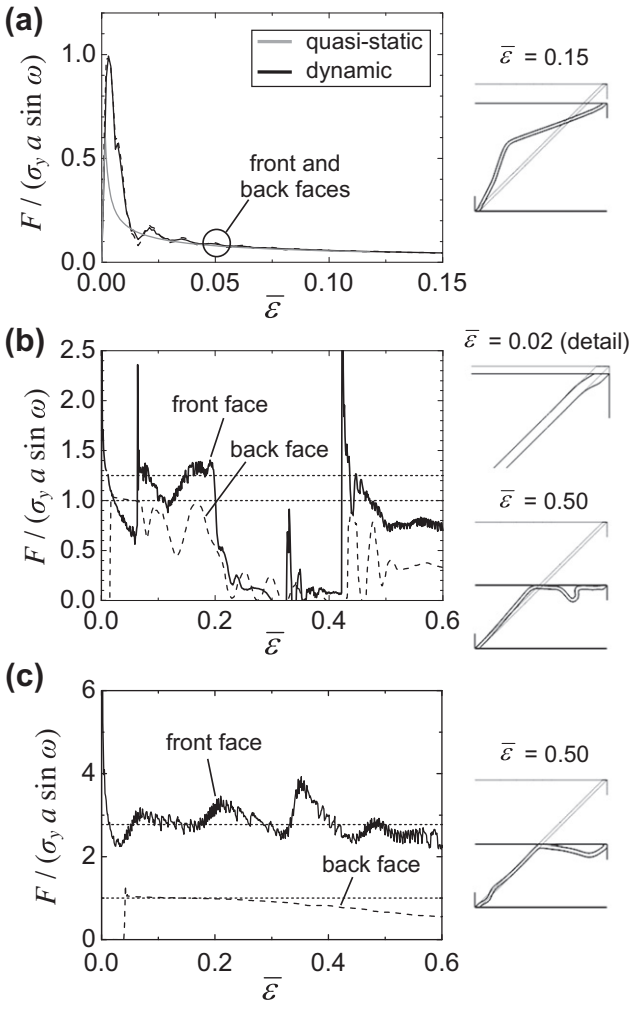

Fig. 3. Variation in the face sheet reaction force F during dynamic collapse of the corrugated core with $L/a = 60$, and $V_0/(c_{pl} \sin \omega)$ equal to (a) 0.0083, (b) 0.50 and (c) 1.3. The quasi-static result is also plotted in (a). Selected deformed shapes are shown adjacent to the corresponding plot. The predictions of the 'stubbing' model for the front and back faces (Eqs. (6) and (7)) are shown as dotted lines in (b) and (c). Non hardening plasticity.

strut, this mode is indistinguishable from the quasi-static mode. However, for the slender strut, we observe that the buckling direction at $V_0/(c_{pl} \sin \omega) = 8.3 \times 10^{-3}$ is opposite to the quasi-static case (and opposite to the direction of the initial geometric imperfection). We attribute this reversal in the buckling direction to inertial effects. In each case, the middle hinge contacts a face sheet at $\bar{\varepsilon} = 0.3 - 0.4$, and results in a sudden increase in force, as seen in Fig. 2a. (This lock-up feature is absent from Fig. 3a, as the scale has been expanded to emphasise the early response.)

(2) *Buckle-waves*. As the velocity is increased, axial plastic wave propagation affects the buckling mode in a similar manner to that described by Vaughn and Hutchinson (2006). In this regime, the buckle wavelength is limited by the length over which the axial plastic wave has propagated, hence the term 'buckle-wave'. However, there is a fundamental difference in the behaviour observed here for inclined struts and that observed by Vaughn and Hutchinson (2006) for the vertical strut: interference of the inclined strut with the front face sheet interrupts the full development of an axial buckle-wave, as the strut folds against the moving front face. We refer to this as 'stubbing' collapse. During stubbing, both front and back face sheet reaction forces remain approximately constant with time. The front face reaction force is higher than the back, due to the inertial contribution of the material folded against the moving face sheet.

Figs. 2b and 3b show results for the inclined strut at a front face sheet velocity $V_0/(c_{pl} \sin \omega) = 0.5$ (equivalent to $V_0 = 60\ \mathrm{ms}^{-1}$) for aspect ratios $L/a = 20$ and 60, respectively. The front and back face forces are not equal indicating that the struts are no longer in axial equilibrium. Intermittent impact of the buckled strut against the front face gives a spike in the force on the front face (but not on the back face).

Consider first the response for $L/a = 20$. An initial buckle-wave exists at $\bar{\varepsilon} = 0.07$, see the inset of Fig. 2b. This is followed by a stubbing event for $\bar{\varepsilon}$ in the range of 0.2 to 0.4, and then by a second buckling event, as seen in the inset at $\bar{\varepsilon} = 0.5$. We label this sequence of collapse events as B–S–B, where 'B' denotes buckling and 'S' denotes stubbing. Second, consider the collapse sequence for $L/a = 60$. An initial buckle wave occurs for $\bar{\varepsilon} < 0.1$ (see inset of Fig. 3b for $\bar{\varepsilon} = 0.02$) followed by a stubbing event over the range $0.1 < \bar{\varepsilon} < 0.2$. A second buckle then occurs which is again followed by stubbing for $\bar{\varepsilon} > 0.4$. We hence label this collapse sequence as B–S–B–S.

This buckling followed by stubbing is further illustrated in Fig. 4a where we plot the evolution of the equivalent (or von

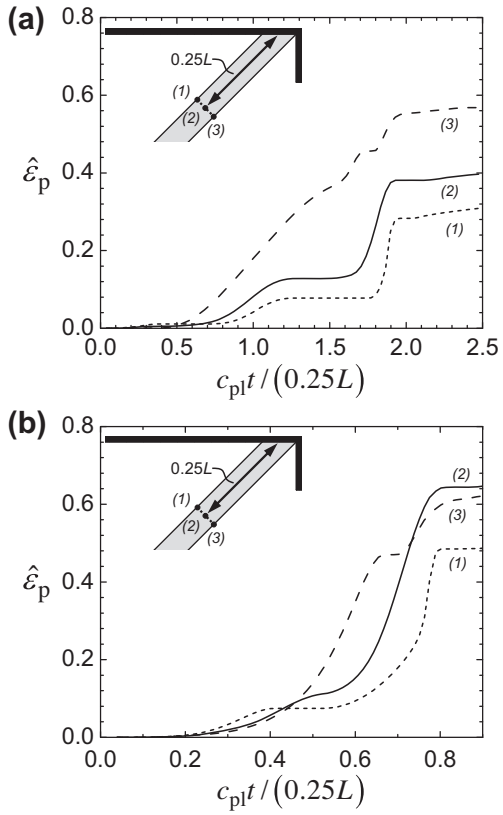

Fig. 4. Time evolution of the equivalent (von Mises) plastic strain at the locations indicated (defined in the undeformed configuration) for the case $L/a = 20$ and $V_0/(c_{pl}\sin\omega)$ equal to (a) 0.50 and (b) 1.3. Non hardening plasticity.

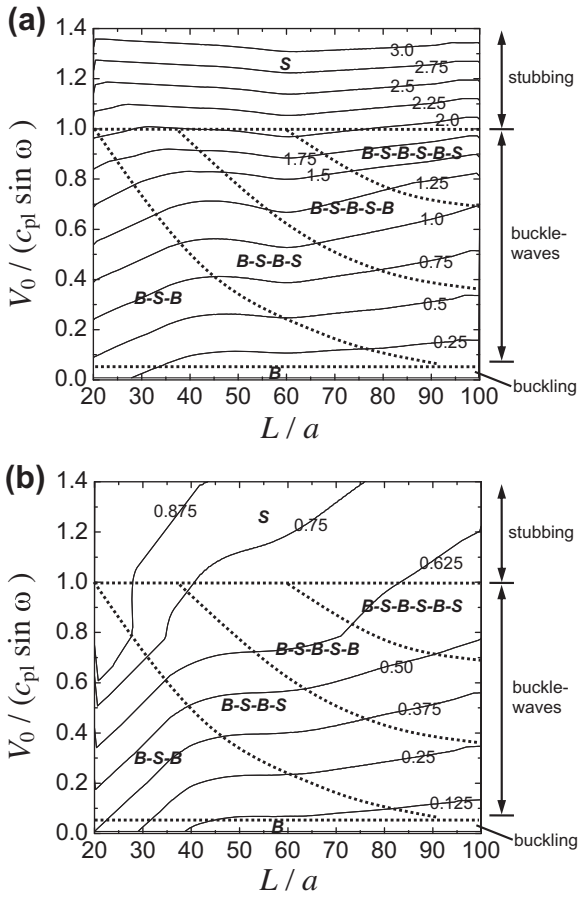

Fig. 5. Collapse mechanism maps with contours of (a) front face average reaction force $\bar{F}_f$ and (b) back face average reaction force $\bar{F}_b$. The dotted lines separate the regimes of collapse. Within each regime, *B* and *S* refer to the phases of buckling and stubbing observed up to $\bar{\varepsilon} = 0.5$. Non hardening plasticity.

Mises) plastic strain with time at a distance $0.25L$ from the impacted face for the $L/a = 20$ strut impacted at a normalised velocity $V_0/(c_{pl}\sin\omega) = 0.5$. The plastic strains are plotted for points on the inner and outer surface of the strut and at mid-section as illustrated in the inset in Fig. 4a. It is clear from Fig. 4a that the plastic wave does not arrive at the measurement location as a sharp front but rather as a diffuse front with plastic deformation commencing at a normalised time $c_{pl}t/L \approx 0.125$ and continued plastic straining occurring until $c_{pl}t/L \approx 0.5$. This is attributed to the fact that the plastic wave comprises both longitudinal and bending waves that travel at different velocities resulting in the observed diffused front. Further, the plastic strains at the three points along the cross-section of the strut differ confirming that the strut is undergoing axial shortening as well as bending. At time $c_{pl}t/L \approx 0.5$, the front face reaches the measurement location resulting in stubbing and the plastic strain thereafter remains reasonably constant.

(3) *Stubbing only*. At higher compression velocities the collapse is dominated by the 'stubbing' mode. Figs. 2c and 3c show results for the inclined strut compressed at a front face sheet velocity $V_0/(c_{pl}\sin\omega) = 1.3$ (equivalent to $V_0 = 160\ \mathrm{ms}^{-1}$) for aspect ratios $L/a = 20$ and 60, respectively. In this regime there are no buckling events: the strut stubs against the moving face sheet throughout the deformation. Deformed meshes at $\bar{\varepsilon} = 0.5$ are shown in Figs. 2c and 3c. This regime is observed for $V_0/(c_{pl}\sin\omega) \geqslant 1$ (up to the highest velocity considered in this study). At these velocities, the axial plastic wave is unable to propagate ahead of the moving front face sheet. The initial bucklewave is therefore suppressed. For $L/a = 20$ and 60, both the front and back face reaction forces remain approximately constant with time.

A simple analytical expression for the front face stubbing force F_f can be obtained by a momentum and mass balance and is given by:

$$\frac{F_f}{\bar{\sigma}_Y a\sin\omega} = 1 + \frac{\rho V_0^2}{\bar{\sigma}_Y \sin^2\omega}, \tag{6}$$

where ρ is the density. The back-face force F_b is deduced by assuming that the non-stubbed portion of the strut is at axial compressive yield, and thus the vertical force on the back face is given by

$$\frac{F_b}{\bar{\sigma}_Y a\sin\omega} = 1. \tag{7}$$

The above analysis is the plane strain, inclined-strut variant of the Taylor analysis for axial impact of a rod, Taylor (1948). A detailed derivation of Eqs. (6) and (7) is provided in the Appendix. The predictions of Eqs. (6) and (7) have been added to Figs. 2 and 3, and show good agreement with the calculated face sheet reaction forces during stubbing collapse.

Following Fig. 4a, we plot the evolution of the plastic strains for the $L/a = 20$ strut impacted at $V_0/(c_{pl}\sin\omega) = 1.3$ in Fig. 4b. Here the front face arrives at the measurement location at a normalised time $c_{pl}t/L \approx 0.2$. In contrast to Fig. 4a we clearly see that there is significantly less plastic straining or bending before the arrival of the front face at the measurement location. This confirms that at $V_0/(c_{pl}\sin\omega) = 1.3$ the $L/a = 20$ strut is in the stubbing only regime with negligible buckle wave effects.

3.2. Collapse mechanism maps

We now summarise the velocity and slenderness dependence of the collapse modes in the form of collapse mechanism maps, with

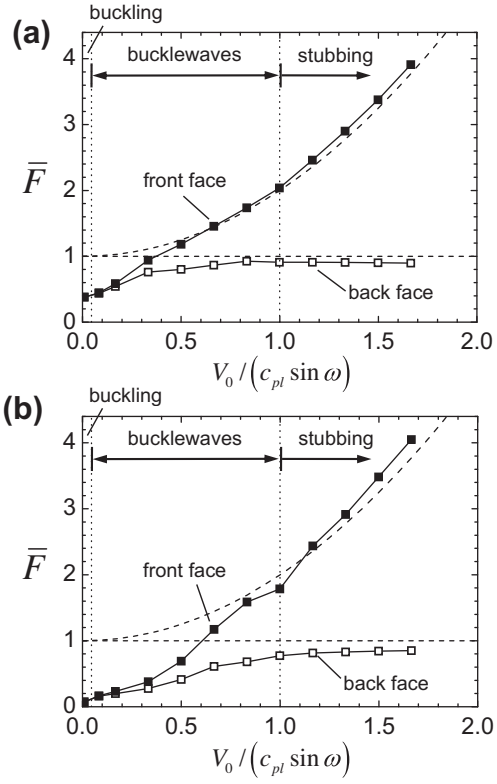

Fig. 6. Variation in average reaction force $\overline{F}$ with velocity for a slenderness (a) $L/a = 40$ and (b) $L/a = 60$. The predictions of the 'stubbing' model for the front and back faces (Eqs. (6) and (7)) are shown as dashed lines. The regimes of collapse are indicated. Non-hardening plasticity.

axes of $V_0/(c_{pl} \sin \omega)$ and L/a. Separate maps are given to show the average front face force $\langle F_f \rangle$ and back face force $\langle F_b \rangle$, obtained by averaging from a core compression $\bar{\varepsilon} = 0$ up to $\bar{\varepsilon} = 0.5$. The maps in Fig. 5 display contours of normalised force such that

$$\overline{F}_f \equiv \frac{\langle F_f \rangle}{\bar{\sigma}_Y a \sin \omega} \quad \text{and} \quad \overline{F}_b \equiv \frac{\langle F_b \rangle}{\bar{\sigma}_Y a \sin \omega}. \tag{8}$$

The key features of the collapse mechanism maps are as follows.

The elastic/plastic buckling regime (labelled *B* in Fig. 5) is restricted to the lowest compression velocities, $V_0 (c_{pl} \sin \omega)^{-1} \leqslant 0.05$, and exists over the full range of slenderness ratios considered. At higher velocities, collapse is by buckle-waves, entailing a sequence of buckling (B) and stubbing (S). The number of buckling and stubbing events observed up to $\bar{\varepsilon} = 0.5$ increases with increasing impact velocity and slenderness ratio, and this is illustrated by B–S–B, B–S–B–S and so on within Fig. 5. For $V_0/(c_{pl} \sin \omega) \geqslant 1$, collapse is by stubbing alone.

To gain further insights into the velocity dependence of the average face sheet reaction forces, two 'slices' through the regime map at $L/a = 20$ and 60 are plotted in Fig. 6. The three regimes of collapse are indicated. In broad terms, the front and back face forces increase with increasing velocity. The presence of stubbing leads to a divergence between front and back face forces at $V_0/(c_{pl} \sin \omega) > 0.2$. Slenderness ratio has only a mild effect upon these forces, particularly for $V_0/(c_{pl} \sin \omega) > 0.5$. The quadratic divergence of front face and back face forces is consistent with the predictions of Eqs. (6) and (7). Indeed, the predictions by this analytical stubbing model are shown to be in excellent agreement with the finite element predictions for $V_0/(c_{pl} \sin \omega) > 1$.

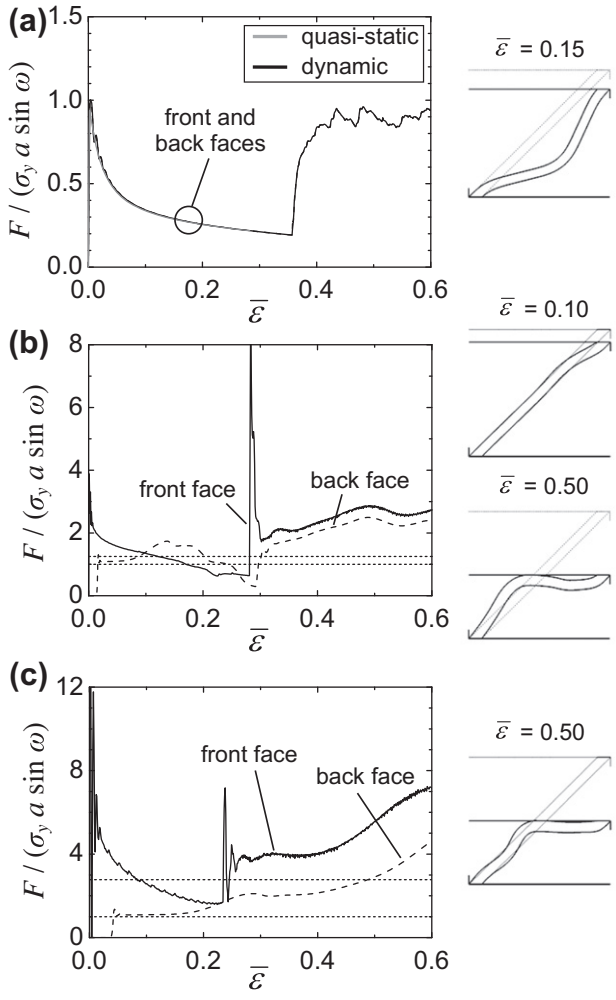

Fig. 7. Variation in the face sheet reaction force F during dynamic collapse of the corrugated core with $L/a = 20$, and $V_0/(c_{pl} \sin \omega)$ equal to (a) 0.0024, (b) 0.15 and (c) 0.39. The quasi-static result is also plotted in (a). Selected deformed shapes are shown adjacent to the corresponding plot. The predictions of the 'stubbing' model for the front and back faces (Eqs. (6) and (7)) are shown as dotted lines in (b) and (c). Strain hardening plasticity.

4. Collapse response for a strain hardening solid

We now consider the influence of strain hardening upon the compressive collapse of the corrugated core with inclination angle $\omega = 45°$. The initial yield strength ($\sigma_y = 200$ MPa) remains unchanged, but now the material hardens with constant tangent modulus $E_t = E/100 = 2$ GPa, as outlined in Section 2. The plastic wave speed is now given by:

$$c_{pl} = \sqrt{\frac{E_t}{\rho}} = 500 \text{ ms}^{-1}, \tag{9}$$

whereas for the non-hardening case we recall that $c_{pl} = \sqrt{\sigma_Y/\rho} = 158$ ms^{-1}. (Note that under plane strain conditions these values become $\sqrt{\bar{E}_t/\rho} = 577$ ms^{-1} and $\sqrt{\bar{\sigma}_y/\rho} = 170$ ms^{-1}, respectively). Consequently, stubbing is limited to higher velocities.

4.1. Selected collapse responses

We again perform calculations with compression velocities in the range $V_0 = 1$–200 ms^{-1}, identical to Section 3. The higher

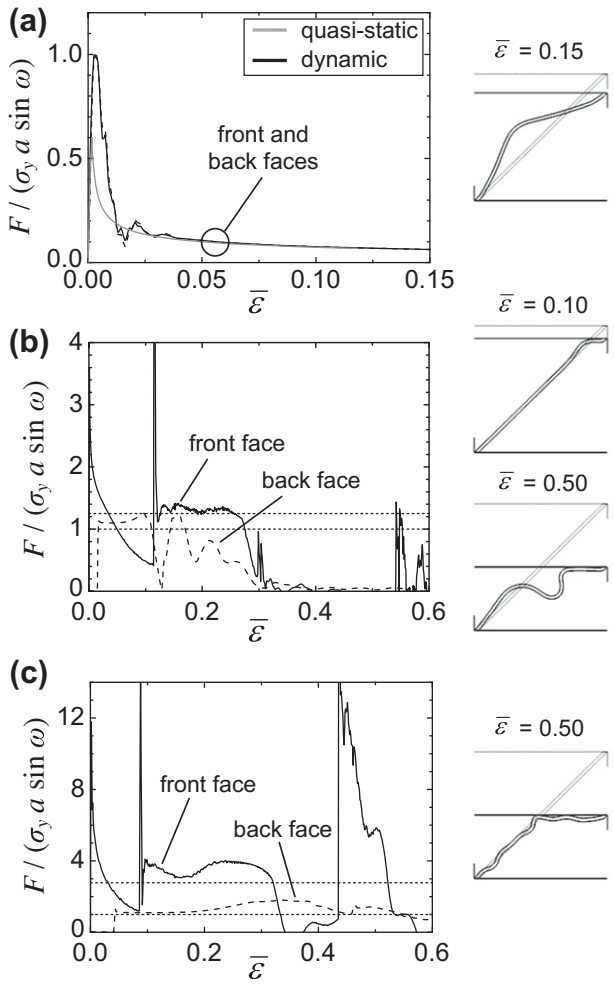

Fig. 8. Variation in the face sheet reaction force F during dynamic collapse of the corrugated core with $L/a = 60$, and $V_0/(c_{pl} \sin \omega)$ equal to (a) 0.0024, (b) 0.15 and (c) 0.39. The quasi-static result is also plotted in (a). Selected deformed shapes are shown adjacent to the corresponding plot. The predictions of the 'stubbing' model for the front and back faces (Eqs. (6) and (7)) are shown as dotted lines in (b) and (c). Strain hardening plasticity.

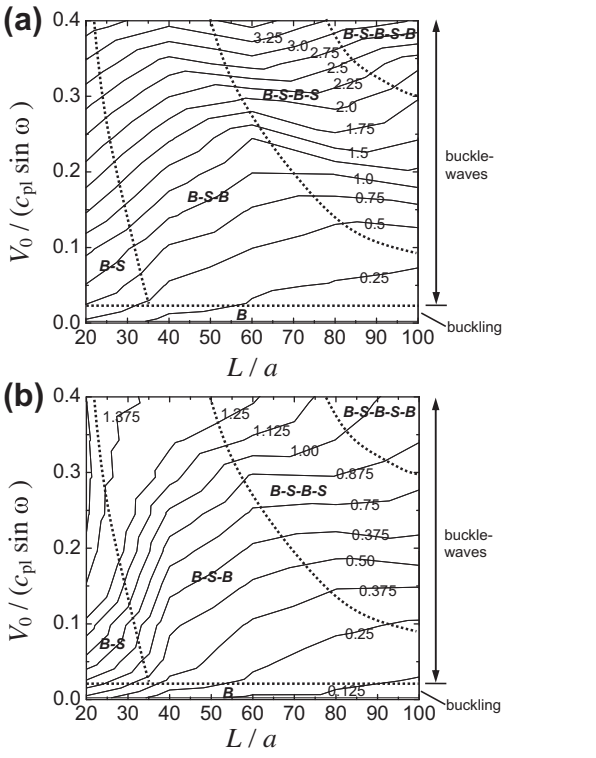

Fig. 9. Collapse mechanism maps with contours of (a) front face average reaction force $\bar{F}_f$ and (b) back face average reaction force $\bar{F}_b$. The dotted lines separate the regimes of collapse. Within each regime, *B* and *S* refer to the phases of buckling and stubbing observed up to $\bar{\varepsilon} = 0.5$. Strain hardening plasticity.

plastic wave speed implies that the normalised deformation velocity range is now $V_0/(c_{pl} \sin \omega) = 2.4 \times 10^{-3} - 0.49$. Quasi-static calculations are also performed. The collapse force history and observed modes are plotted in Fig. 7 for a stocky strut of aspect ratio $L/a = 20$ ($\bar{\rho} = 9\%$) and in Fig. 8 for a slender strut of aspect ratio $L/a = 60$ ($\bar{\rho} = 3\%$). In each figure, the responses are shown for the same absolute value of velocity as reported in Figs. 2 and 3: $V_0 = 1$, 60 and 160 ms^{-1}.

At low compression velocities, $V_0 = 1\ \text{ms}^{-1}$, the strut collapses by plastic buckling, as for the case of ideal plasticity, see Figs. 7 and 8a. The quasi-static response also mimics that for ideal plasticity. At intermediate and high velocities, $V_0/(c_{pl} \sin \omega)$ equal to 0.15 and 0.39 (corresponding to $V_0 = 60$ and 160 ms^{-1}), collapse is by buckle-waves, involving a sequence of buckling and stubbing. Specifically, the stocky strut ($L/a = 20$) collapses in a B–S mode (see Fig. 7b, c), whereas the slender strut ($L/a = 60$) collapses in a B–S–B mode at $V_0/(c_{pl} \sin \omega) = 0.15$ and in a B–S–B–S at $V_0/(c_{pl} \sin \omega) = 0.39$ (see Fig. 8b, c). Note that the impact velocities considered were not sufficiently high for $V_0/(c_{pl} \sin \omega)$ to exceed unity and for stubbing alone to occur. The predictions of the stubbing model, Eqs. (6) and (7), have been added to Figs. 7 and 8. Strain hardening results in higher face sheet reaction forces during the stubbing phases of collapse than predicted by Eqs. (6) and (7).

4.2. Collapse mechanism map

Finite element calculations for a wide range of compression velocities and aspect ratios have again been assembled into a collapse mechanism map, Fig. 9, analogous to that shown in Fig. 5 for the case of ideal plasticity. The regimes of collapse are shown, along with contours of normalised front force ($\bar{F}_f$) and back force ($\bar{F}_b$), see Fig. 9a and b, respectively.

Only two regimes appear in Fig. 9 as we have limited our attention to the range $V_0/(c_{pl} \sin \omega) < 0.4$: buckling only (marked *B* in the figure) and a buckle-wave regime, comprising alternating buckling and stubbing (marked *B* and *S*). Compared to the non-hardening case (Fig. 5) across the same range of normalised velocity $V_0/(c_{pl} \sin \omega)$, an additional subdivision (*B*–*S*) appears at low L/a for the hardening strut.

5. Strain rate sensitivity

We complete the study by considering the role of strain rate sensitivity. We adopt a strain rate dependent material behaviour representative of type 304 stainless steel, as specified in Section 2. For struts compressed uniaxially, strain rate sensitivity smears out plastic shocks over a finite width and thereby leads to the possibility of scale effects: the collapse response may depend upon the structural size in comparison with this plastic shock width.

In this section we consider the influence of strain rate sensitivity on the dynamic buckling response of the inclined strut. Three strut configurations are considered.

(i) A 'model scale' strut of thickness $a = 1$ mm. The material strain hardens but has negligible strain rate sensitivity as assumed in Section 4.

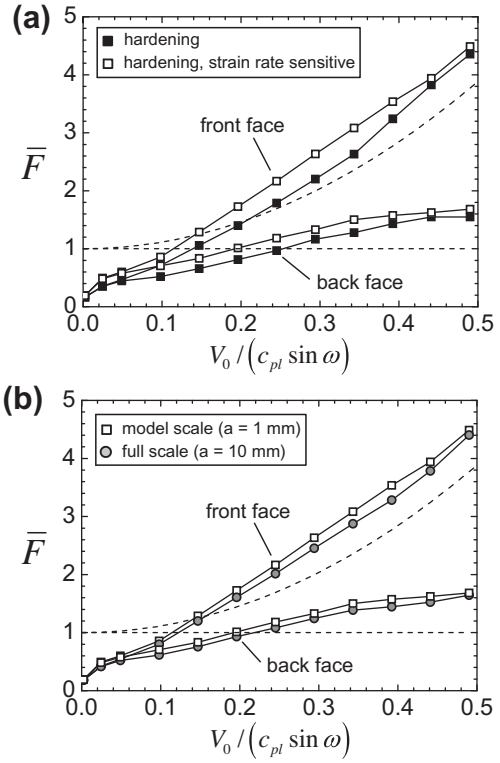

Fig. 10. Variation in average reaction force $\overline{F}$ with velocity for a slenderness $L/a = 40$. The predictions of the 'stubbing' model for the front and back faces (Eqs. (6) and (7)) are shown as dashed lines. (a) Strain hardening plasticity with low strain rate sensitivity, and strain hardening plasticity with strain rate sensitivity representative of 304 stainless steel. (b) Strain hardening, strain rate sensitive plasticity for two sizes of model: $a = 1$ mm and $a = 10$ mm.

(ii) A 'model scale' strut of thickness $a = 1$ mm. The material strain hardens and has the strain rate sensitivity $R(\dot{\varepsilon}_{pl})$ representative of stainless steel, as defined in Section 2.

(iii) A 'full scale' strut of thickness $a = 10$ mm with the same constitutive description as in (ii). Note that in these calculations, the same element size is employed as for the 'model scale' in order to maintain the same number of elements across the shock width.

The influence of strain-rate sensitivity on the front and back face sheet average reaction forces $\overline{F}$ is shown in Fig. 10a for a strut of aspect ratio $L/a = 40$. Cases (i) and (ii) are compared. Strain rate sensitivity increases the average reaction force at both the front and back face sheets across the full range of compression velocities. The effect of structural dimension is shown in Fig. 10b, where cases (ii) and (iii) are compared. Increasing the size of the strut by a factor of ten reduces the collapse strength only slightly. This gives confidence in the direct applicability of laboratory scale test data on the dynamic buckling response of corrugated cores to their full-scale analogues.

6. Conclusions

Finite element analysis has been used to investigate the dynamic collapse of a single inclined strut compressed at constant velocity between rigid face sheets. This strut represents an idealised unit cell of a metallic lattice sandwich core as might be used in blast protection applications. The material model is representative of stainless steel, with strain hardening and strain rate sensitive plasticity introduced systematically. The time evolution of plastic collapse is assessed and the effect of compression velocity and strut slenderness (i.e. core relative density) determined.

Three classes of collapse mode have been identified as a function of impact velocity: (i) a three-hinge plastic buckling mode of wavelength equal to the strut length, similar to the quasi-static mode, (ii) a 'buckle-wave' regime involving inertia-mediated plastic buckling of wavelength less than that of the strut length, and (iii) a 'stubbing' regime, with shortening of the struts by local fattening at the front face. The force on the front face due to the collapsing strut exceeds that on the back face force for collapse modes (ii) and (iii). This is traced to the plastic shock across the stubbed portion of the strut. The presence of strain hardening increases the plastic wave speed and reduces the degree of stubbing. In contrast, strain rate sensitivity has a much more mild effect upon the collapse response.

Acknowledgements

The authors are grateful for financial support from the US Office of Naval Research.

Appendix A. Derivation of reaction forces for the stubbing deformation mode

Consider a corrugated core made from a rigid-ideally plastic solid as sketched in Fig. A1 under plane strain compression. This core is compressed at a velocity $V_0 > c_{pl} \sin \omega$ so that plastic deformation is concentrated in the vicinity of the front face. The FE calculations suggest that the mode of deformation is as sketched in Fig. A1. We derive an estimate for the front and back face forces using mass and momentum conservation as follows.

At time $t = 0$, the front face sheet is moved with a constant velocity V_0. Because of the rigid nature of the initial response of the corrugated core material, we assume that the entire strut is immediately brought to axial yield and thus the vertical component of the force on the back face is given by

$$F_b = \bar{\sigma}_Y a \sin \omega. \tag{A1}$$

For the deformation mode sketched in Fig. A1, a momentum balance dictates that the vertical component of force on the front face is given as

$$F_f = F_b + \frac{d}{dt}[\ell \rho a V_0], \tag{A2}$$

where we have employed the fact that F_b is time invariant. In Eq. (A2) ℓ is the length of the strut that has stubbed against the front

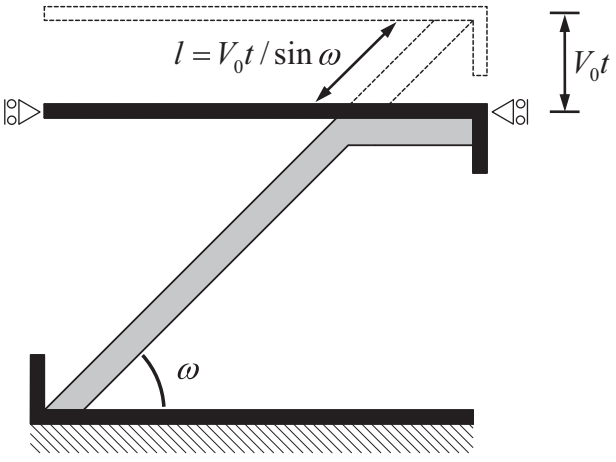

Fig. A1. Geometry of the collapsed strut assumed for the stubbing mode model.

face sheet as shown in Fig. A1. At time t, the geometry of the deformed strut dictates that

$$\ell = \frac{V_0 t}{\sin\omega}. \tag{A3}$$

Hence, it follows from Eqs. (A1)–(A3) that the front face force

$$F_f = \bar{\sigma}_Y a \sin\omega + \frac{V_0^2 \rho a}{\sin\omega}. \tag{A4}$$

References

Abrahamson, G.R., Goodier, J.N., 1966. Dynamic flexural buckling of rods within an axial plastic compression wave. Journal of Applied Mechanics 33, 241–247.

Calladine, C.R., English, R.W., 1984. Strain-rate and inertia effects in the collapse of two types of energy absorbing structures. International Journal of Mechanical Sciences 26, 689–701.

Côté, F., Deshpande, V.S., Fleck, N.A., Evans, A.G., 2006. The compressive and shear responses of corrugated and diamond lattice materials. International Journal of Solids and Structures 43, 6220–6242.

Deshpande, V.S., Fleck, N.A., 2000. High strain rate compression behaviour of aluminium alloy foams. International Journal of Impact Engineering 24, 277–298.

Ferri, E., Antinucci, E., He, M.Y., Hutchinson, J.W., Zok, F.W., Evans, A.G., 2006. Dynamic buckling of impulsively loaded prismatic cores. Journal of the Mechanics of Materials and Structures 1, 1345–1366.

Fleck, N.A., Deshpande, V.S., 2004. The resistance of clamped sandwich beams to shock loading. Journal of Applied Mechanics 71, 386–401.

Hoff, N.J., 1951. The dynamics of the buckling of elastic columns. Journal of Applied Mechanics 18 (1), 68–74.

Hönig, A., Stronge, W.J., 2000. Dynamic buckling of an imperfect elastic, visco-plastic plate. International Journal of Impact Engineering 24 (9), 907–923.

Jones, N., 1989. Structural Impact. Cambridge University Press, Cambridge.

Jones, N., 2003. Several phenomena in structural impact and structural crashworthiness. European Journal of Mechanics A/Solids 22, 693–707.

Karagiozova, D., Jones, N., 1995. A note on the inertia and strain-rate effects in the Tam and Calladine model. International Journal of Impact Engineering 16 (4), 637–649.

Karagiozova, D., Jones, N., 1996. Dynamic elastic-plastic buckling phenomena in a rod due to axial impact. International Journal of Impact Engineering 18 (7-8), 919–947.

Lee, S., Barthelat, F., Hutchinson, J.W., Espinosa, H.D., 2006. Dynamic failure of metallic pyramidal truss core materials – Experiments and modelling. International Journal of Plasticity 22, 2118–2145.

Radford, D.D., Deshpande, V.S., Fleck, N.A., 2005. The use of metal foam projectiles to simulate shock loading on a structure. International Journal of Impact Engineering 31, 1152–1171.

Radford, D.D., Fleck, N.A., Deshpande, V.S., 2006. The response of clamped sandwich beams subjected to shock loading. International Journal of Impact Engineering 32, 968–987.

Radford, D.D., McShane, G.J., Deshpande, V.S., Fleck, N.A., 2007. Dynamic compressive response of stainless-steel square honeycombs. Journal of Applied Mechanics 74, 658–667.

Rathbun, H.J., Radford, D.D., Xue, Z., He, M.Y., Yang, J., Deshpande, V., Fleck, N.A., Hutchinson, J.W., Zok, F.W., Evans, A.G., 2006. Performance of metallic honeycomb-core sandwich beams under shock loading. International Journal of Solids and Structures 43, 1746–1763.

Reid, S.R., 1993. Plastic deformation mechanisms in axially compressed metal tubes used as impact energy absorbers. International Journal of Mechanical Sciences 35 (12), 1035–1052.

Stout, M.G., Follansbee, P.S., 1986. Strain-rate sensitivity, strain hardening and yields behaviour of 304L stainless steel. Journal of Engineering Materials Technology 108, 344–353.

Su, X.Y., Yu, T.X., Reid, S.R., 1995a. Inertia-sensitive impact energy absorbing structures, Part I: Effects of inertia and elasticity. International Journal of Impact Engineering 16 (4), 651–672.

Su, X.Y., Yu, T.X., Reid, S.R., 1995b. Inertia-sensitive impact energy absorbing structures, Part II: Effect of strain rate. International Journal of Impact Engineering 16 (4), 673–689.

Tan, P.J., Reid, S.R., Harrigan, J.J., Zou, Z., Li, S., 2005a. Dynamic compressive strength properties of aluminium foams. Part I – Experimental data and observations. Journal of the Mechanics and Physics of Solids 53 (10), 2174–2205.

Tan, P.J., Reid, S.R., Harrigan, J.J., Zou, Z., Li, S., 2005b. Dynamic compressive strength properties of aluminium foams. Part II – 'Shock' theory and comparison with experimental data and numerical models. Journal of the Mechanics and Physics of Solids 53 (10), 2206–2230.

Taylor, G.I., 1948. The use of flat-ended projectiles for determining dynamic yield stress. I. Theoretical considerations. Proceedings of the Royal Society A 194, 289–299.

Tilbrook, M.T., Radford, D.D., Deshpande, V.S., Fleck, N.A., 2007. Dynamic crushing of sandwich panels with prismatic lattice cores. International Journal of Solids and Structures 44, 6101–6123.

Vaughn, D.G., Canning, J.M., Hutchinson, J.W., 2005. Coupled plastic wave propagation and column buckling. Journal of Applied Mechanics 72, 139–146.

Vaughn, D.G., Hutchinson, J.W., 2006. Bucklewaves. European Journal of Mechanics A/Solids 25, 1–12.

Xue, Z., Hutchinson, J.W., 2004. A comparative study of blast-resistant metal sandwich plates. International Journal of Impact Engineering 30, 1283–1305.

Xue, Z., Hutchinson, J.W., 2006. Crush dynamics of square honeycomb sandwich cores. International Journal for Numerical Methods in Engineering 65, 2221–2245.